Cold-resonance-mediated self-stabilization of Kerr frequency combs in a Si_3N_4 microring resonator

Sauradeep Kar,[1,*] Maitrayee Saha,[2] Saawan Kumar Bag,[3] Rajat K. Sinha,[4] Shubhanshi Sharma,[1] Sridhar Singhal,[1] and Shailendra K. Varshney[1,†]

[1]*Department of Electronics and Electrical Communication Engineering, Indian Institute of Technology, Kharagpur 721302, India*

[2]*Department of Physics, Indian Institute of Technology, Kharagpur 721302, India*

[3]*The Alexander Kofkin Faculty of Engineering, Bar-Ilan University, Ramat Gan 5290002, Israel*

[4]*Department of Electrical and Computer Engineering, University of Toronto, Toronto, Ontario, Canada M5S*

(Received 4 March 2022; revised 26 May 2022; accepted 15 June 2022; published 19 July 2022)

Kerr frequency combs (KFCs) generated from continuous-wave pumped microresonators have been vastly exploited for a plethora of applications. Along with an appreciable bandwidth, most of the applications demand a stable and coherent frequency comb, which is a challenging quest. Several complex experimental approaches were reported to attain stable frequency combs. In this paper, we report an innovative and simple approach to achieve stabilized KFCs in a Si_3N_4 racetrack microring resonator. Intensive numerical simulations reveal an enhancement of the comb bandwidth when the temperature is reduced slightly lower than the room temperature. The maximum temperature rise due to the propagating dissipative Kerr soliton (DKS) has also been studied through finite element simulations. Through homogeneous steady-state analysis we validate that the stability of a single DKS state is enhanced at the temperatures reported in this paper. We believe that the proposed thermal route may help in reducing the complex experimental procedures for stabilization of KFCs.

DOI: 10.1103/PhysRevA.106.013517

I. INTRODUCTION

Temporally localized ultrashort optical pulses, commonly known as dissipative Kerr solitons (DKSs) [1], manifest as equidistant frequency lines called Kerr frequency combs (KFCs) in the frequency domain. Interplay between dispersion and nonlinearity, triggered by cascaded four wave mixing (FWM), is the predominant mechanism responsible for generation of frequency combs [2,3]. KFCs sustained by parametric gain from FWM have been studied in all optical fiber cavities [4] as well as in microresonators [5]. On chip microresonator based KFCs [6–8] are robust in nature. Due to their robustness such KFCs can be utilized in the development of optical atomic clocks with unparalleled stability [9,10], optical frequency synthesizers [11,12], and generation of microwave frequency signals with low phase noise [13]. Moreover, KFCs spanning in the mid IR frequency range have shown the ability to detect gas at ppb level [14], thereby justifying their significant contributions in the area of spectroscopy as well.

Along with a wide spectral bandwidth, various applications demand generation of coherent and stable KFCs [15]. The common practice to generate stable KFCs has been the utilization of single DKS states [5]. Such DKS states are generated by sweeping the pump frequency over a range of wavelengths which in turn changes the detuning between the pump and the cavity resonant wavelength [15]. This leads to traversal of the pump frequency through chaotic regions and the stable DKS is determined probabilistically. The stable DKS states tend to align on the red detuned side of the resonator's pump resonance mode [16], where thermo-optical (TO) effects cause a major hindrance to access stable soliton states [17]. Thermal detuning modifies the refractive index of the resonator material and hence influences the optical power circulating within the resonator [18]. Thus, thermo-optical effects may play a major role in controlling the stability of the DKS and hence the microcomb. Macroscale whispering gallery mode (WGM) resonators like MgF_2 crystalline devices [5] and silica (SiO_2) microresonators [19] exhibit a slow thermal time constant [20] which facilitates generation of favorable stable DKS states through a gradual adjustment of the pump laser frequency to the appropriate detuning level. Self-thermal-locking has been reported in WGM resonators for small fluctuations in the pump energy whereby a stable DKS state can be obtained [17]. Still, in the absence of a stabilizing circuitry [21,22], it becomes difficult to sustain the DKS state in such resonators as well.

Several approaches have been proposed to link the pump frequency to the resonator line. A self-injection-locking procedure has been reported in [23] where a passive feedback mechanism realizes the concept of thermal stability of the resonance condition in WGM resonators. In on chip integrated microresonator platforms the thermal time constant is much faster [24], due to which it becomes really cumbersome to access stable DKS states through a gradual sweep of the pump laser frequency as the quality of the frequency comb crucially depends on the linewidth and the amplitude noise of the pump. Usage of tunable lasers is not a good alternative in such a situation as devices tend to be inherently noisy and have a broad linewidth (typically of the order of 100 kHz) [25]

*dhruba12@iitkgp.ac.in

†skvarshney@ece.iitkgp.ac.in

than fixed wavelength lasers. Several resonance tuning techniques have been proposed to control the detuning between the pump and the resonance mode to obtain a sustained and stable DKS state by using a fixed wavelength pump laser. Integrated heaters capable of allowing fast thermal tuning of the resonance wavelength at a time scale much shorter than the thermal relaxation time of the resonator have been reported in both the normal [26] and anomalous [27] dispersion regimes to generate stable DKS states and coherent broadband frequency combs. The fast response time of the heaters plays an important role to achieve consistent and reliable generation of the frequency comb state.

A stabilization scheme of the DKS state has been reported in [28] that involves an additional auxiliary microring resonator in an external fiber loop cavity possessing optical gain. A single resonance of the microcavity synchronizes with the resonance of the fiber loop and is amplified. This amplified resonance is then passively fed back to the resonator that acts as a pump in order to generate stable DKS states. Also, it becomes important to ensure that the generated stable DKS state remains unperturbed to effects caused by the drift of the resonance wavelength due to thermal effects [25]. In order to maintain the soliton state against thermal drift, a method of simultaneous dynamic control of the pump laser frequency and power has been proposed [19,29]. This mechanism of "servo" control of the pump monitors the soliton output power, providing soliton sustenance over long durations. Furthermore, usage of single sideband modulators [30], phase modulation of the pump [31], and usage of an additional auxiliary laser for temperature compensation [32] have been proposed as techniques to obtain stable DKS states. The aforementioned techniques involve very complex optical circuitry. Methods to obviate such techniques involve usage of resonators with low optical absorption [33], or by operation at cryogenic temperatures [34].

The present paper provides an innovative and simple solution to attain stable DKSs and hence KFCs in a silicon nitride (Si_3N_4) racetrack microring resonator (RMRR). Through numerical simulations of the well-known Lugiato-Lefever equation (LLE) that governs the dynamics of DKSs in a resonator system, the effect of temperature on the generated DKS and hence the frequency comb has been studied in depth. The necessary parameters for the LLE to generate stable DKSs have been extracted through finite difference time domain (FDTD) and finite element method (FEM) simulations. FEM simulations yield the maximum temperature excursion within the resonator due to the circulating DKS. The maximum temperature value has also been confirmed through analytical evaluation of the rate equation that dictates the temperature change within the mode volume of the resonator [35]. An interesting behavior in the frequency comb bandwidth is observed as the temperature reduces slightly. The spectral density of thermorefractive noise has been estimated for the proposed resonator at room temperature, at a chosen temperature that is slightly lower than the room temperature and at a cryogenic temperature of 100 K. It is evident from such calculations that the proposed solution can be a potential alternative to generation of KFCs at cryogenic temperatures. Homogeneous steady-state (HSS) analysis predicts the stable soliton state, which conforms with the numerical predictions. The extensive study presented in this paper and the conclusions drawn aid in generating stable and sustained DKS states in microresonators at slightly low temperatures with respect to room temperature.

II. MODAL CHARACTERISTICS OF THE PROPOSED RMRR

Figure 1(a) shows the schematic top view of the proposed RMRR whereas the inset depicts the cross-sectional view. The bus and the ring waveguides are made of Si_3N_4. The waveguide width and height are 2.8 and 0.7 μm, respectively. The outer ring radius (R) is 50 μm and each of the straight arms of the ring has a length $L_c = 120$ μm. The geometry is simulated using the commercially available Lumerical FDTD solver. A gap of 400 nm between the bus and the ring facilitates the operation in a slightly overcoupled regime [36]. The FEM is used to obtain dispersion and nonlinear properties of the waveguide. Figure 1(b) shows the normalized electric-field distribution of the fundamental TE mode at a wavelength of 1.560 14 μm. Figure 2(a) depicts the dispersion, D, and the group velocity dispersion (GVD), β_2, parameters. The waveguide exhibits three zero dispersion points at 1, 1.74, and 2.67 μm. At a pump wavelength of 1.560 μm, the group velocity dispersion is -174.9 ps^2/km. Such low second-order GVD, β_2, enhances the KFC bandwidth by producing short DKSs along with spectral coherence [37]. The other requisite parameters such as effective mode area (A_{eff}) and the nonlinear parameter (γ) [37] have been depicted in Fig. 2(b). The waveguide exhibits effective Kerr nonlinearity, $\gamma = 0.65$ W^{-1} m^{-1}, at the pump wavelength of 1560 nm. Another important parameter that characterizes the extinction and the resonance characteristic of RMRR is the coupling

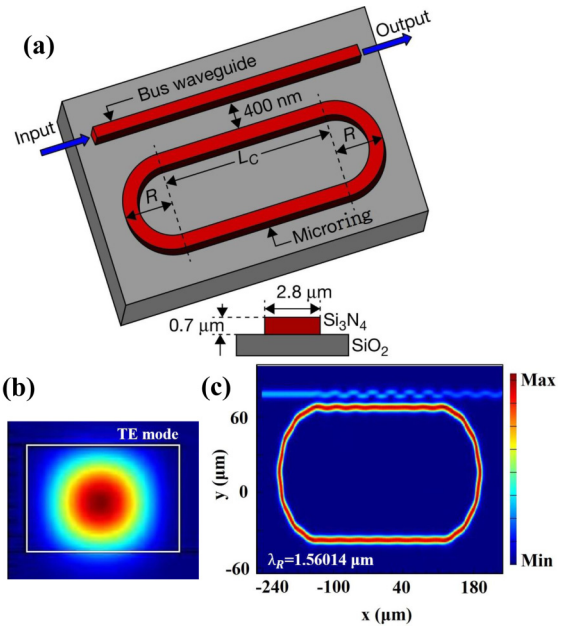

FIG. 1. (a) Schematic of the proposed RMRR, $R = 50$ μm, and straight arm length, $L_c = 120$ μm. Inset: Resonator cross section of the waveguide. (b) Normalized electric-field distribution of the fundamental TE mode. (c) Electric field within the resonator at resonance wavelength $\lambda_R = 1.56$ μm.

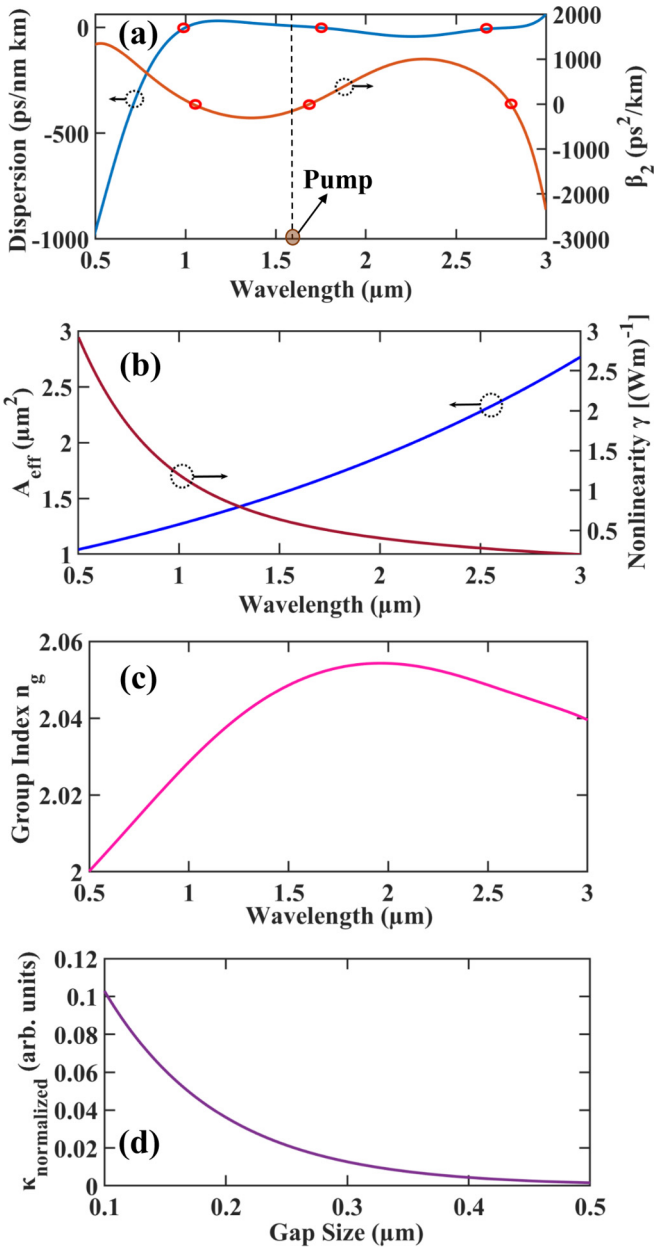

FIG. 2. Modal characteristics of the Si_3N_4 waveguide. (a) Dispersion (D) and second-order GVD (β_2) (red circles correspond to the zero dispersion points; the dotted line denotes the pump wavelength). (b) Spectral variation of the effective mode area (A_{eff}) and nonlinear parameter (γ). (c) Group index. (d) Variation of the normalized coupling coefficient ($\kappa_{\text{normalized}}$) as a function of gap separation.

coefficient, κ, between bus and ring waveguides which has been evaluated numerically by solving an overlap integral [38]:

$$\kappa_{pq} = \frac{\omega\epsilon_0 \int_{-\infty}^{\infty}\int_{-\infty}^{\infty}\left(N^2 - N_q^2\right)E_p^* E_q dxdy}{\int_{-\infty}^{\infty}\int_{-\infty}^{\infty} u_z.(E_p^* \times H_p + E_p \times H_p^*)dxdy}. \quad (1)$$

In Eq. (1) the bus and ring waveguides are demarcated by indices p and q, corresponding to which the electric and magnetic fields of the modes in the individual waveguides are designated as E_p/E_q and H_p/H_q. The refractive indices of the individual waveguides are demarcated as N_p and N_q and the refractive index of the entire coupled waveguide is denoted as N. Here u_z is the unit vector in the z direction, by considering the electromagnetic wave propagation in the z direction. The variation of the normalized coupling coefficient ($\kappa_{\text{normalized}}$) with the gap size is exhibited in Fig. 2(d). The coupling coefficient is normalized with respect to the cavity length. The coupling coefficient decreases with an increase in the gap size due to poor evanescent field coupling into the ring waveguide. The spectral variation of the group index (n_g) is displayed in Fig. 2(c).

III. ROOM-TEMPERATURE KFC SIMULATIONS

Numerical simulations of the Kerr frequency comb have been carried out by the well-known externally driven and damped nonlinear Schrödinger equation which describes the mean-field dynamics of the cavity. This equation is popularly known as the LLE [39–41], given below:

$$t_R\frac{\partial E}{\partial t} = \left[-\left(\frac{\alpha+\kappa}{2}\right) - i\delta_0 + iL\sum_{m\geqslant 2}\frac{\beta_m}{m!}\left(i\frac{\partial}{\partial\tau}\right)^m + i\gamma L|E|^2\right]E + \sqrt{\kappa}E_{\text{in}} \quad (2)$$

where t_R represents the round trip time, and $E\ (t,\tau)$ and E_{in} are the intracavity field and input fields, respectively. t is the slow time which denotes the time for field confinement within the resonator in accordance with the photon lifetime. τ is the fast time which symbolizes the behavior of the temporal envelope of the signal that moves at the group velocity. The slow and fast times are linked to the index m, which indicates the number of round trips traversed by the field in the cavity, by the relation $E(t = mt_R, \tau) = E^{(m)}(0,\tau)$. δ_0 is the cavity phase detuning defined as $\delta_0 = t_R(\omega_n - \omega_0)$ where ω_0 and ω_n are the pump's angular frequency and the frequency of the nth resonant mode. α, κ, γ, and β_m represent the power loss per round trip, the power coupling coefficient, the nonlinear coefficient, and the mth-order dispersion coefficient. L represents the circumference of the cavity. The normalized parameters are

$$\alpha' = \frac{\alpha+\kappa}{2}, \quad t' = \alpha\frac{t}{t_R}, \quad \tau' = \tau\sqrt{\frac{2\alpha'}{|\beta_2|L}},$$

$$E' = E_{\text{in}}\sqrt{\frac{\gamma L}{\alpha'}}, \quad S = E_{\text{in}}\sqrt{\frac{\gamma L\kappa}{\alpha'^3}}, \quad D = \frac{\delta_0}{\alpha'}.$$

Equation (2) can be recast in normalized form as

$$\frac{\partial E'}{\partial t'} = \left[-1 + iD + i\frac{\partial^2}{\partial\tau'^2} - i|E'|^2\right]E' + S. \quad (3)$$

FDTD numerical simulations of RMRR yield round trip loss α (normalized with respect to the cavity length), of 3.4×10^{-3}, when a unity power is launched at the input port of the resonator.

The coupling coefficient for 400-nm gap separation between the bus and ring waveguides is 4.45×10^{-3}. The cavity round trip time (t_R) is defined as $t_R = \frac{2n_{\text{eff}}L}{c}$, where n_{eff} is the

TABLE I. Simulation parameters for KFC generation.

Parameter	Values
Pump wavelength (λ_0)	1560 nm
Resonant wavelength (λ_R)	1560.14 nm
Round trip time (t_R)	4.455 ps
Cavity detuning (δ_0)	0.065 rad
Round trip loss (α)	0.0034
Coupling coefficient ($\kappa_{\text{normalized}}$)	0.0044538
Second-order GVD (β_2)	-174.9 ps^2/km
Third-order dispersion (β_3)	-0.318 ps^3/km
Nonlinear parameter (γ)	0.65 W^{-1}m^{-1}
Input power (P_{in})	265 mW

effective refractive index of the mode. For a cavity length $L = 554.16\,\mu$m, the round trip time (t_R) is 4.45 ps. The simulated field profile at the resonance condition of the proposed resonator is shown in Fig. 1(c). The simulations are carried out in Lumerical FDTD by exciting the input port of the bus waveguide with a TE polarized light. In simulations, the dispersive nature of materials is taken into account, through the Sellmeier equation for silicon nitride (Si_3N_4) and silica (SiO_2) [42]. Perfectly matched layer boundary conditions are used in the simulation region. The computational time is set to 10 ns to ensure proper convergence of simulation results. Figure 3(a) depicts the transmission spectrum at the through port of the resonator. The asymmetric extinction ratio in transmission dips is due to material dispersion. From Fig. 3(a), it is evident that if the pump wavelength is $1.560\,\mu$m, then resonance occurs at a wavelength of $1.560\,14\,\mu$m rendering a cavity phase detuning, $\delta_0 = 0.065$. It is seen through HSS analysis [40] that for this detuning value, an input power $P_{\text{in}} = |E_{\text{in}}|^2 = 0.265$ W can successfully generate stable single DKS states. Further details on HSS analysis are given later in Sec. VII. The simulation parameters are summarized in Table I. Equation (2) is solved numerically where the temporal window is chosen in such a way that it coincides with the round trip time t_R, generating uniform frequency grids spaced by free spectral range (FSR). To solve Eq. (2), the functional form of the steady-state solution of the same has been used as an initial field, which can be approximated by the following analytical expression [36]:

$$E_{\text{initial}}(\tau) = E_{\text{in}} + \sqrt{\frac{2\delta_0}{\gamma L}}\, e^{i\phi_0}\, \text{sech}\left(\sqrt{\frac{2\delta_0}{|\beta_2|L}}\,\tau\right) \tag{4}$$

where

$$\phi_0 = \cos^{-1}\left(\frac{\alpha}{E_{\text{in}}}\sqrt{\frac{8\delta_0}{\pi\gamma L\kappa}}\right). \tag{5}$$

The temporal cavity soliton and the corresponding frequency comb are shown Figs. 3(b) and 3(c), respectively. When we incorporate third-order dispersion ($\beta_3 = \frac{\partial\beta_2}{\partial\tau}$) along with β_2, the comb bandwidth spans over an octave [Fig. 3(c)]. Although the typical Cherenkov-like resonant dispersive wave emission [37] at the longer wavelength could not be observed for the computed parameters for this design, still the asymmetric envelope of the comb and the octave

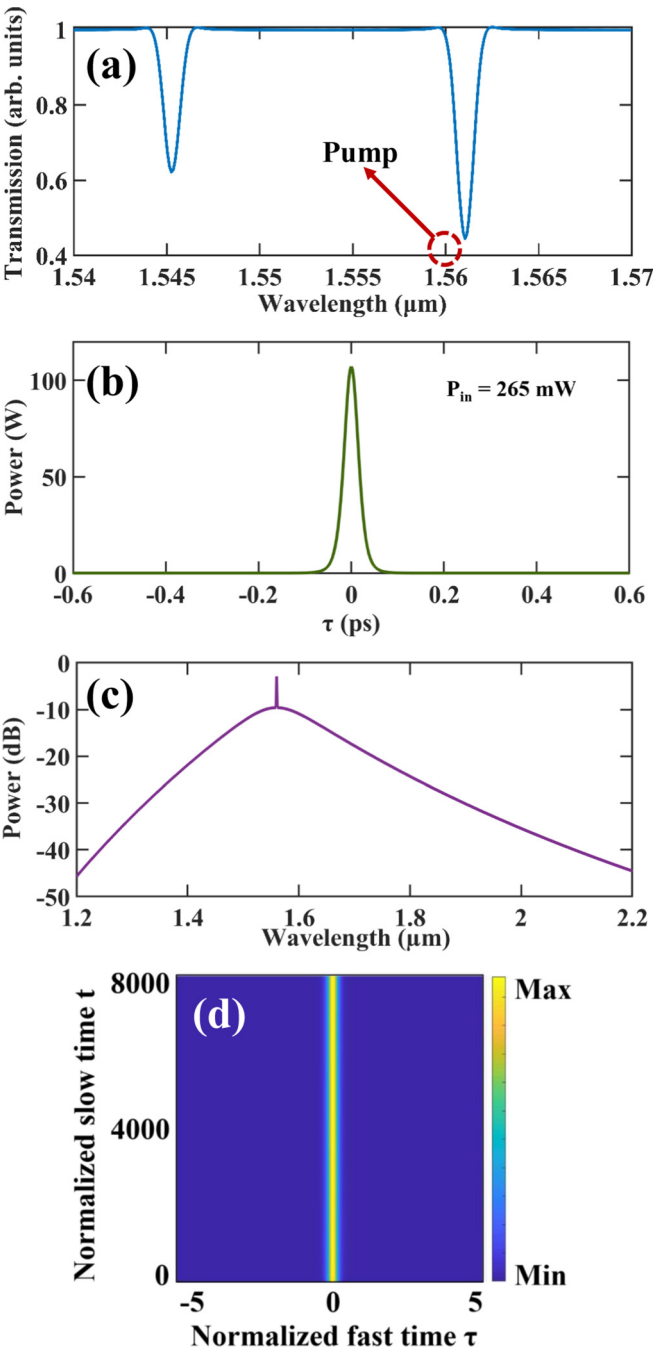

FIG. 3. (a) Transmission spectrum of the RMRR. (b) Temporal cavity soliton at an input pump power of 265 mW. (c) Frequency comb in the presence of both β_2 and β_3. (d) Mesh plot illustrating the steady-state field confinement.

spanning bandwidth are reasonably in agreement with previously published results [36,43]. Figure 3(d) represents the field evolution, confirming sustained cavity soliton propagation.

IV. THEORETICAL ANALYSIS OF THE KFC AT LOW TEMPERATURE

The LLE portrayed in Eq. (2) does not take into account the TO effect. To address thermal effects, we adopt the

TABLE II. Thermal rates obtained from COMSOL.

Parameter	Values
Effective thermal relaxation rate (Γ_m)	0.853333×10^2 Hz
Effective optical absorption rate (γ_m)	8.89 K/J

procedure illustrated in [35], and the traditional form of LLE in Eq. (2) has been modified. The solution of Eq. (2) provides the circulating field $E(t,\tau)$. Note that the associated parameters are valid for the room-temperature operation. Thus, the field $E(t,\tau)$ calculated in the first iteration is the circulating field of the temporal solitonic state at room temperature. The thermo-optical effect occurs when the local temperature of the mode volume changes. We make use of the following rate equation [44] to model thermal effects:

$$\frac{d\Delta T_m}{dt} = -\Gamma_m \Delta T_m + \gamma_m (|E(t,\tau)|^2)_{\text{avg}}. \tag{6}$$

In Eq. (6), the variable t represents the slow time and ΔT_m corresponds to the maximum temperature change with respect to room temperature due to the circulating DKS. $(|E(t,\tau)|^2)_{\text{avg}}$ is the average intensity of the circulating DKS at room temperature which is obtained from Eq. (2). Γ_m and γ_m are the effective thermal relaxation and optical absorption rates of the fundamental mode in the resonator [45], which we calculate from COMSOL MULTIPHYSICS which is an FEM solver. All necessary values are given in Table II.

By solving Eq. (6), we get $\Delta T_m = 30$ K, which is the maximum possible positive temperature change after which the stable solitonic state can no longer be accessed [45]. Any further increase in temperature does not cause the solitonic state to remain stable. In order to study the frequency comb dynamics in the cold resonance regime, the same value of temperature gradient is considered but with an opposite sign, i.e., $\Delta T = -30$ K. Under such situation, the blueshift in resonance wavelength is given by

$$\Delta\lambda = \lambda_0 \left(\frac{dn_0}{dT} \frac{\Delta T}{n_0} \right). \tag{7}$$

Here, $\frac{dn_0}{dT}$ is the thermo-optical coefficient of Si_3N_4 at a temperature T. Typical values of thermo-optical coefficient data have been taken from experimental values given in [46]. The shift in resonance wavelength, calculated through FDTD simulations at low temperatures, provides the detuning. In order to theoretically validate the calculated resonance wavelength shift, the temperature-dependent refractive index is considered in simulations as

$$n_{Si_3N_4/SiO_2} = n(\Delta T = 0K) + \Gamma_{Si_3N_4/SiO_2} \Delta T. \tag{8}$$

$\Gamma_{Si_3N_4/SiO_2}$ denotes the thermo-optical coefficient of silicon nitride–silica. Figure 4(a) shows the transmission spectrum at room temperature and at temperatures lower than the room temperature, viz., $\Delta T = -30, -40$, and -50 K. The detuning values deduced for the room temperature and lower temperatures for a pump wavelength of 1560 nm are given in Table III.

We observe that temperature change (ΔT) also induces a variation in effective mode area (A_{eff}) and nonlinear parameter (γ), as shown in Fig. 4(b). It is seen that the nonlinearity

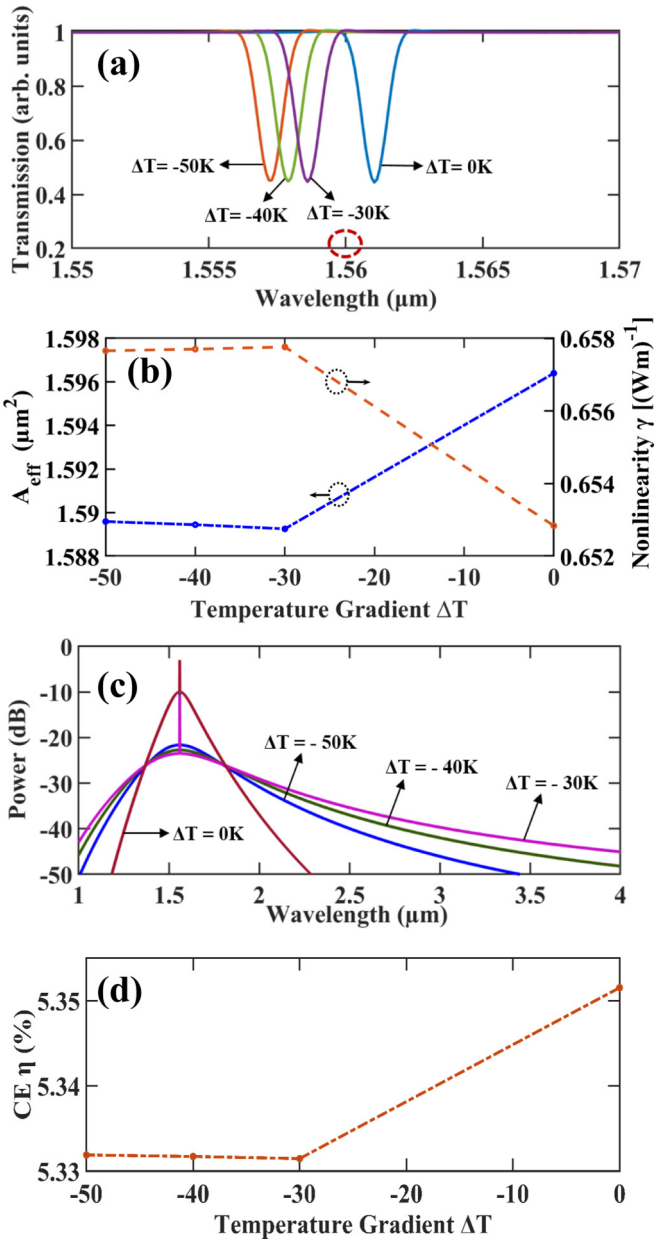

FIG. 4. (a) Transmission spectrum (the pump wavelength has been encircled), (b) effective mode area and nonlinearity, (c) frequency comb, and (d) nonlinear conversion efficiency at various temperature values. The temperature is presented as changes in the temperature with respect to room temperature.

enhances at lower temperatures, with a maximum value at a temperature gradient of -30 K. The detuning values, given in Table III, and the nonlinear parameter values at the respective temperatures have been plugged into the LLE, to obtain the Kerr frequency comb at low temperatures. However, no significant change has been observed in dispersion and coupling coefficient at low temperatures, indicating that the thermo-optical effect is only dominant at such temperatures with negligible thermal expansion effect. The KFCs at the room and chosen low temperatures is shown in Fig. 4(c). Interestingly, the comb bandwidth enhances as the temperature decreases and the maximum comb bandwidth occurs at

TABLE III. Detuning values at different temperature gradients.

Pump wavelength λ_0 (μm)	Resonance wavelength λ_R (μm)	Type	Detuning $\lvert\delta_0\rvert = \lvert t_R(\omega_0 - \omega_R)\rvert$ (rad)	Temperature gradient ΔT (K)
1.56	1.56012	Hot	0.0659	0
	1.5586	Cold	0.7696	−30
	1.5579	Cold	1.155	−40
	1.5572	Cold	1.541	−50

$\Delta T = -30$ K. We believe this enhancement in comb bandwidth is due to increased γ, leading to enhanced four wave mixing that results in generation of new frequency components (see the Appendix for details).

To corroborate these findings, we calculate the nonlinear conversion efficiency (CE) [47,48] which is a measure of the degree to which the power contained in the CW pump can distribute among different frequency lines spanned over the entire bandwidth range of the frequency comb. A large value of nonlinear conversion efficiency is desirable as it yields a uniform distribution of the pump power over different frequency components of a frequency comb. According to recent studies [48], the nonlinear conversion efficiency can be evaluated by considering a steady-state continuous-wave solution of Eq. (2) (i.e., $\frac{\partial}{\partial t} = \frac{\partial}{\partial \tau} = 0$). The steady-state solution of Eq. (2) is given by $E_{SS}(\delta_0) = \frac{\sqrt{\kappa}E_{in}}{(\alpha + i\delta_0)}$, where the symbols have their usual meanings. The steady-state output at the through port of the ring resonator can be written as $E_{out}(\delta_0) = E_{in} - \sqrt{\kappa}E_{SS}(\delta_o)$. Accordingly, the nonlinear conversion efficiency (η) (near critical coupling $\kappa = \alpha$) is given by the following relation [48]:

$$\eta = \pi \sqrt{\frac{c\alpha|\beta_2|(1 \mp \sqrt{r})^3}{\gamma E_{in} n_g (1 \pm \sqrt{r})}} \sqrt{\text{FSR}} \tag{9}$$

where $r = [\frac{E_{out}(\delta_0 \to 0)}{E_{out}(\delta_0 \to \infty)}]^2 = [1 - (\frac{\kappa}{\alpha})^2]$ is the on-resonance normalized output power, and n_g is the group index of the propagating mode. The other symbols have their usual meaning as elucidated earlier. The nonlinear conversion efficiency at various temperature gradients is plotted in Fig. 4(d). It is seen that the conversion efficiency is maximum at the room temperature (i.e. $\Delta T = 0$ K). It follows from an obvious consequence that at room temperature the frequency comb bandwidth as well as nonlinear parameter are minimum, compared to other temperature values. Nevertheless, the CE value at all temperatures is greater than 5.3% which is reasonably good in comparison to the published values [48] yielding a considerably flat frequency comb. It is evident that the CE can be affected by coupling coefficient [Eq. (9)] which is controlled by the gap separation. In contrast to this, the nonlinear conversion efficiency can be tailored by varying the temperature for a fixed gap separation.

V. FEM ANALYSIS OF DKS INDUCED TEMPERATURE CHANGE

The magnitude of temperature rise within the resonator due to the circulating DKS has been understood through FEM simulations. From a very rudimentary concept of heat transfer in solids, it can be stated that

$$Q(x, y, z) = n_{imag} I(x, y, z) \tag{10}$$

where $Q(x, y, z)$ is the energy absorbed by any material at a point when the intensity at that point is $I(x, y, z)$. n_{imag} is the imaginary part of the refractive index of the material. For Si_3N_4, n_{imag} is 3×10^{-5} [42] at 1.56 μm. It has been reported in [25] that a circulating optical field in a resonator with peak intensities greater than 1 GW/cm^2 can lead to significant increase in temperature. The DKS reported in Fig. 3(b) has a peak intensity of 7.14 GW/cm^2 which is large enough to increase the temperature locally. The circulating DKS has been modeled as a moving heat source that traverses the microring in a round trip time of 4.45 ps. For simulation, the circular portion of the ring has been considered only, because thermal effects tend to shift the resonance wavelength of the resonator and the inclusion of the straight arms in the racetrack configuration does not create a major shift in the resonance wavelength. The incident heat flux from the circulating cavity soliton is modeled as a spatially distributed heat source, which has a mathematical form specifying the Gaussian distribution of the DKS state. The heat source rotates along the perimeter of the resonator with a time period equal to the round trip time of the circulating cavity soliton. In order to simulate the heat source, a moving mesh is employed. The overall energy absorbed or the heat load due to the circulating DKS is then obtained in accordance to Eq. (10). The temperature values have been stored at every computational step. Figure 5(a) shows the temperature

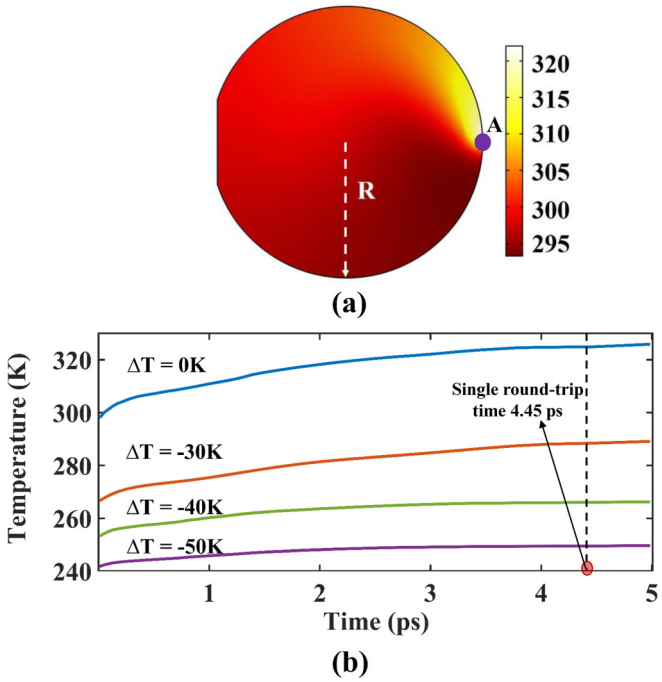

FIG. 5. (a) Top view of the RMRR indicating growth of the temperature gradient when a Gaussian pulse with a peak power of 100 mW is fed into the RMRR with radius $R = 50$ μm. (b) Temperature rise as a function of round trip time for $\Delta T = 0$, −30, −40, and −50 K.

distribution across the ring waveguide. The geometrical center of the resonator has been chosen as the reference point for the heat source, hence an intersection between the geometry of the moving heat source and the ring has resulted in the visual representation of the structure shown in the aforementioned figure.

In numerical simulations, the heat source is made to traverse one round trip along the circumference of the ring from the reference position A, as shown in Fig. 5(a), giving rise to maximum temperature excursion, $\Delta T_m \approx 30$ K, with respect to room temperature ($T = 293$ K). Numerical simulations for various initial temperature values 263 K ($\Delta T = -30$ K), 253 K ($\Delta T = -40$ K), and 243 K ($\Delta T = -50$ K) yield a maximum temperature change, $\Delta T_m \approx 25$, 13, and 8 K, respectively, for one round trip, as depicted in Fig. 5(b). We find that the temperature excursion stays less than 30 K for temperatures of 263, 253, and 243 K, which indicates that the stable single DKS state and hence the frequency comb can be easily sustained at such temperatures. Numerical simulation results show an excellent agreement with the theoretical values for the temperature excursion as reported in the previous section.

VI. THERMOREFRACTIVE NOISE CALCULATIONS

It is well known that the resonance frequencies of the different modes of the MRR strongly depend on the material refractive index. The thermo-optical effect causes a change in the refractive index due to thermal fluctuations which result in frequency noise. The average fluctuation in temperature of the MRR is given by [49]

$$\left\langle (\delta T)^2_{\mathrm{MRR}} \right\rangle = \frac{k_B T^2}{C_P V_m \rho} \tag{11}$$

where C_P is the specific-heat capacity, V_m is the mode volume, and ρ is the density of the resonator's material. Thermal fluctuations also influence the radius of the resonator, but in our context such effects have been ignored because of negligible thermal expansion coefficient. The change in the resonance frequency of the resonator due to thermal fluctuations manifests as the spectral density of optical fluctuations [34]:

$$S_f = (f_0 n^{-1} \Gamma_{\mathrm{Si_3N_4}})^2 S_{T_{\mathrm{MRR}}}(\omega) \tag{12}$$

where $f_0 = \frac{c}{\lambda_0} = 192.30$ THz is the frequency of the pumped mode, $\Gamma_{\mathrm{Si_3N_4}}$ is the thermo-optical coefficient of silicon nitride, and $S_{T_{\mathrm{MRR}}}(\omega)$ is the spectral density of thermal fluctuations. $S_{T_{\mathrm{MRR}}}(\omega)$ has been calculated by the approximation of the thermal decomposition method for a thin resonator [49]:

$$S_{T_{\mathrm{MRR}}}(\omega) = \frac{k_B T^2 R^2}{12 \kappa_T V_m} \left[1 + \left(\frac{R^2 \rho C_p \omega}{9\sqrt{3}\kappa_T} \right)^{\frac{3}{2}} + \frac{1}{6} \left(\frac{R^2 \rho C_p \omega}{8 \nu^{\frac{1}{3}} \kappa_T} \right)^2 \right]^{-1}. \tag{13}$$

Here, T is the absolute temperature in Kelvin, R is the radius of the MRR, κ_T is the thermal conductivity of the material, ω is the Fourier frequency, and ν is the azimuthal mode order of the pumped fundamental mode. The parameters used for evaluation of S_f from Eq. (12) are given in Table IV.

TABLE IV. Parameters used for thermorefractive noise calculation.

Parameter	Values
Pump frequency (f_0)	192.30 THz
Thermal conductivity (κ)	30 W m^{-1} K^{-1} [34]
Mode volume (V_m)	1.5602×10^{-16} m^{-3} ($T = 293$ K)
	1.0209×10^{-16} m^{-3} ($T = 263$ K)
	1.0109×10^{-16} m^{-3} ($T = 253$ K)
	1.0032×10^{-16} m^{-3} ($T = 243$ K)
	1×10^{-16} m^{-3} ($T = 100$ K)
MRR radius (R)	50 μm
Density (ρ)	3.29×10^3 kg m^{-3} [34]
Specific heat capacity (C_p)	800 J kg^{-1} K^{-1} [34]
Mode number (ν)	627

The mode volume (V_m) has been calculated through FEM simulations. Based on the above-mentioned parameters, the spectral density of optical fluctuations is calculated for the room temperature ($T = 293$ K, $\Delta T = 0$ K), and for $T = 263$ K ($\Delta T = -30$ K), $T = 253$ K ($\Delta T = -40$ K), $T = 243$ K ($\Delta T = -50$ K), and $T = 100$ K ($\Delta T = -193$ K). The normalized spectral density $\frac{\sqrt{S_f}}{f_0}$ is plotted for $\Delta T = 0$, -50, and -193 K, respectively, in Fig. 6.

As $\frac{\sqrt{S_f}}{f_0}$ is directly proportional to $(\Gamma_{\mathrm{Si_3N_4}})^2 T^2$, an obvious reduction in the spectral density of optical fluctuations is observed at lower temperatures. This is on par with studies reported at cryogenic temperatures [34]. It can be observed that the spectral density sharply reduces at a frequency of 220 GHz, which is close to the FSR of the MRR. This sharp decrease in $\frac{\sqrt{S_f}}{f_0}$ has been reported [34,49]. It has been seen in the present paper that the spectral density reduces to a small value at the FSR of the cavity (the FSR is encircled in green in Fig. 6). This minimal value of the spectral density is almost equal for the chosen temperature of 243 K ($\Delta T = -50$ K) and at a cryogenic temperature of 100 K ($\Delta T = -193$ K). It is known that the frequency comb lines are primarily spaced at an interval that is numerically equal to the FSR of the cavity. Thus, the spectral density of optical fluctuations is equally low for the primary comb lines at the chosen low temperature of 243 K ($\Delta T = -50$ K) as well as at a cryogenic temperature of 100 K. Hence, it can be reasonably concluded that the

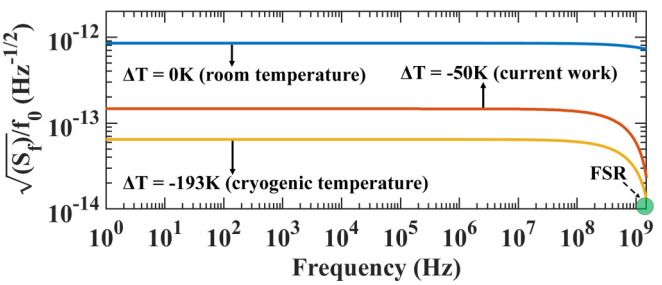

FIG. 6. Calculation of the normalized spectral density of optical fluctuation $\frac{\sqrt{S_f}}{f_0}$ for room temperature ($\Delta T = 0$ K) and lower temperatures ($\Delta T = -50$ and -193 K). The encircled frequency denotes the FSR of the cavity.

chosen temperature regime can aid in sustaining stable DKS states along with KFCs with minimal fluctuations, without necessitating complex cryogenic setups.

VII. COMB SELF-STABILIZATION: HSS ANALYSIS

The normalized LLE solved with the steady-state ($\frac{\partial E'}{\partial t'} = 0$) and homogeneous ($\frac{\partial E'}{\partial \tau'} = 0$) criteria results in the following cubic equation [40]:

$$X = Y^3 - 2Y^2 + (D^2 + 1)Y \tag{14}$$

where $X = |S|^2$, $Y = |E'|^2$, and the rest of the symbols have their usual meanings as elucidated earlier. Clearly, three sets of intracavity field solutions can be obtained from Eq. (14), (i) unconditionally homogeneous stable steady-state solutions, (ii) unconditionally homogeneous unstable solutions, and (iii) conditionally homogeneous stable (oscillatory) solutions. The third type of solution is associated with the phenomenon of modulation instability [37] where a weak periodic perturbation develops on top of the steady-state background both in the anomalous and normal dispersion regimes [37,40] for microring resonators. Equation (14) is a second-order polynomial equation in the normalized detuning D and is trivially solved corresponding to three classes of field solutions as

$$D = Y \pm \sqrt{\frac{X}{Y} - 1}. \tag{15}$$

The solutions of Eq. (15) for the stable, unstable, and oscillatory intracavity field have been depicted in Figs. 7(a) and 7(b) for temperature gradients $\Delta T = 0$ and -30 K. The stable, unstable, and oscillatory solutions are marked by the black points, red asterisks, and green (light gray) circles, respectively. The region of stable field solutions tends to increase while the unstable solutions decrease with the reduction in temperature as seen from Figs. 7(a) and 7(b). The tilt curve depicted in Figs. 7(a) and 7(b) has been plotted for $\Delta T = 30$, 0, -30, -40, and -50 K in Fig. 7(c). It can be clearly seen that a positive temperature excursion from the room temperature ($\Delta T = 30$ K) leads to a rightward tilt and drives the system more towards the red detuned and hence the unstable regime [40]. However, a decrease in the temperature gradient leads to a leftward tilt and enhances the stability of the system by driving the resonance towards the blue detuned side. For better understanding of the impact of change in temperature on the stable and unstable regions, we demarcate the region of unstable solutions due to Kerr nonlinearity in Fig. 8. The shaded regions on the tilt curves clearly establish the evolution of unstable and stable solutions with temperature. Based on HSS analysis, we can conclude that the negative temperature excursion with respect to room temperature leads to higher stability.

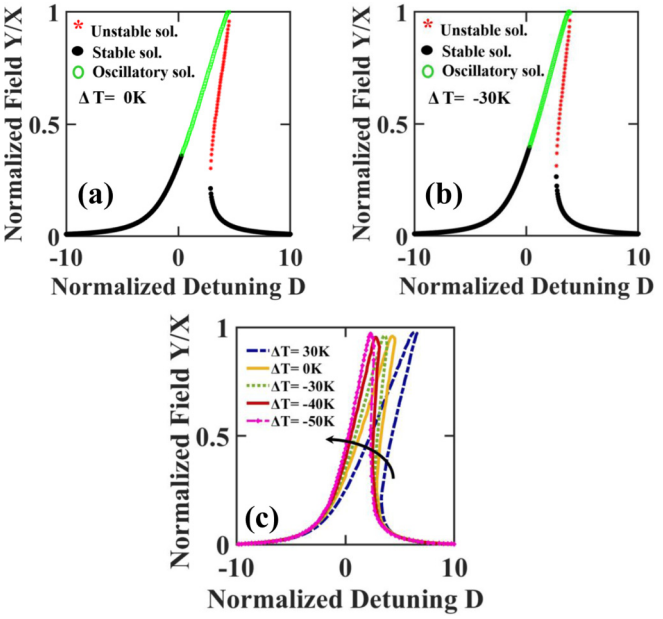

FIG. 7. Kerr tilt curve for (a) $\Delta T = 0$ K and (b) $\Delta T = -30$ K, illustrating various stable (black points), unstable (red asterisks), and oscillatory [green (light gray) circles] solution regions. (c) Kerr tilt for various temperature gradients. The black arrow indicates leftward tilt due to low temperature.

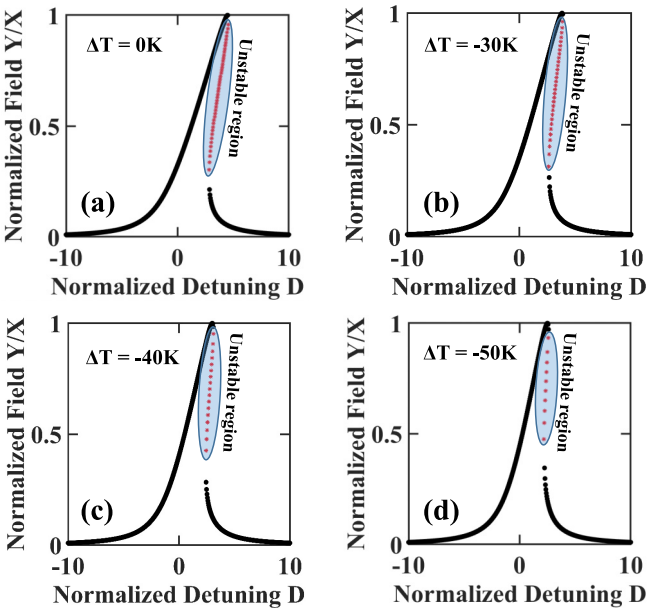

FIG. 8. Kerr tilt curves indicating change in the region of unstable solutions with temperature gradient (ΔT). The shaded region in all four images shows unstable solutions.

VIII. CONCLUSION

In conclusion, we have carried out the study of the single DKS state at temperatures slightly lower than the room temperature in a Si_3N_4 racetrack microring resonator. FEM simulations predict the rise in temperature in a single round trip which is utilized to predict the temperature values at which the maximum excursion in temperature remains less than 30 K. Operating the RMRR below room temperature also results in the enhancement of the comb bandwidth. Detailed FEM, FDTD simulations, and theoretical calculations through the HSS analysis establish that it is easy to sustain the stable frequency comb at such temperatures. Further, the thermorefractive noise is low for the chosen temperature range. The

proposed route to generate KFCs is an easy and simple approach compared to operation at cryogenic temperatures.

ACKNOWLEDGMENT

Authors S.K. and S.K.V. acknowledge the support received from project vide sanction no. DST/NM/NNETRA/2018(6)-IITKGP.

APPENDIX: EFFECT ON KFC 3-dB BANDWIDTH

The empirical formula which gives a good estimate of the 3-dB frequency comb bandwidth is given by the following relation [50]:

$$\begin{aligned}\Delta f_{3\mathrm{dB}_{\mathrm{theoretical}}} &= \frac{0.315}{1.763}\sqrt{\frac{2\gamma P_{\mathrm{in}} Q\lambda_P}{\pi c|\beta_2|t_R}} \\ &= \frac{0.315}{1.763}\sqrt{\frac{2\gamma P_{\mathrm{in}}\mathcal{F}}{\pi|\beta_2|}} \\ &= \frac{0.315}{1.763}\sqrt{\frac{2\gamma P_{\mathrm{in}}}{\alpha|\beta_2|}} \end{aligned} \tag{A1}$$

where Q, λ_P, and t_R are the quality factor of the cavity, pump wavelength, and round trip time, respectively, while the other symbols have their usual meanings. It is well known that the finesse of the resonator is $\mathcal{F} = \frac{\pi}{\alpha} = \frac{Q\lambda_P}{t_R c}$. Thus, it can be reasonably stated that the comb bandwidth predominantly depends on the nonlinear coefficient (γ), input power (P_{in}), round trip loss (α), and second-order group velocity dispersion (β_2), as depicted in Eq. (A1) [50]. Figure 9(a) depicts the change in coupling coefficient (κ) with the gap between the bus and ring waveguides of the MRR at $\Delta T = 0$, -30, -40, and -50 K. There is no significant change in the κ value at the chosen temperature regime, indicating that the thermo-optical effect is only dominant at the reported temperatures with negligible thermal expansion effect. Thus, it is seen that the round trip loss (α) and the second-order group velocity dispersion (β_2) remain fairly constant at the chosen ΔT values, as there is no significant change in the dimensions of the MRR due to minimal thermal expansion effect. An input power $P_{\mathrm{in}} = 265$ mW, evaluated through HSS analysis, is used in the simulations and theoretical calculations. Thus, the parameter which predominantly affects 3-dB comb bandwidth ($\Delta f_{3\mathrm{dB}}$ or $\Delta\lambda_{3\mathrm{dB}}$) is the nonlinear coefficient (γ). The temporal DKS state at $\Delta T = 0$, -30, -40, and -50 K has been depicted in Fig. 9(b). Clearly a decrease in the temporal width of the DKS also aids in enhancing the comb bandwidth at low temperatures. The change in the 3-dB KFC bandwidth ($\Delta\lambda_{3\mathrm{dB}}$) with ΔT is shown in Fig. 9(c).

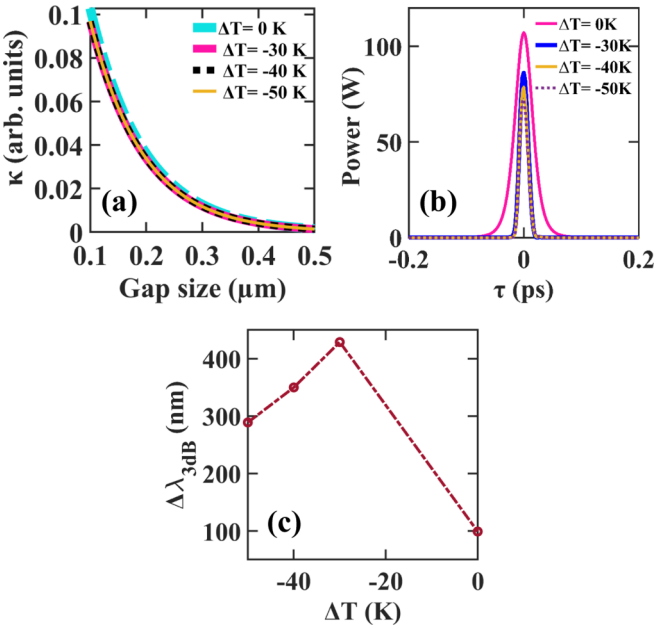

FIG. 9. (a) Variation of the coupling coefficient (κ) as a function of gap separation for various temperature gradient ΔT values. (b) Temporal DKS state for various ΔT values. (c) 3-dB KFC bandwidth $\Delta\lambda_{3\mathrm{dB}}$ as a function of ΔT.

[1] A. Scroggie, W. Firth, G. McDonald, M. Tlidi, R. Lefever, and L. Lugiato, Chaos, Solitons and Fractals **4**, 1323 (1994).

[2] T. J. Kippenberg, R. Holzwarth, and S. A. Diddams, Science **332**, 555 (2011).

[3] P. Del'Haye, A. Schliesser, O. Arcizet, T. Wilken, R. Holzwarth, and T. J. Kippenberg, Nature (London) **450**, 1214 (2007).

[4] F. Leo, S. Coen, P. Kockaert, S.-P. Gorza, P. Emplit, and M. Haelterman, Nat. Photon. **4**, 471 (2010).

[5] T. Herr, V. Brasch, J. D. Jost, C. Y. Wang, N. M. Kondratiev, M. L. Gorodetsky, and T. J. Kippenberg, Nat. Photon. **8**, 145 (2014).

[6] A. Roy, R. Haldar, and S. K. Varshney, J. Lightwave Technol. **36**, 5807 (2018).

[7] Y. Kartashov, O. Alexander, and D. Skryabin, Opt. Express **25**, 11550 (2017).

[8] A. B. Matsko, W. Liang, A. A. Savchenkov, D. Eliyahu, and L. Maleki, Opt. Lett. **41**, 2907 (2016).

[9] A. D. Ludlow, M. M. Boyd, J. Ye, E. Peik, and P. O. Schmidt, Rev. Mod. Phys. **87**, 637 (2015).

[10] T. E. Drake, T. C. Briles, J. R. Stone, D. T. Spencer, D. R. Carlson, D. D. Hickstein, Q. Li, D. Westly, K. Srinivasan, S. A. Diddams, and S. B. Papp, Phys. Rev. X **9**, 031023 (2019).

[11] R. Holzwarth, T. Udem, T. W. Hänsch, J. C. Knight, W. J. Wadsworth, and P. S. J. Russell, Phys. Rev. Lett. **85**, 2264 (2000).

[12] D. T. Spencer, T. Drake, T. C. Briles, J. Stone, L. C. Sinclair, C. Fredrick, Q. Li, D. Westly, B. R. Ilic, A. Bluestone, N. Volet, T. Komljenovic, L. Chang, S. H. Lee, D. Y. Oh, M.-G. Suh, K. Y. Yang, M. H. P. Pfeiffer, T. J. Kippenberg, E. Norberg *et al.*, Nature (London) **557**, 81 (2018).

[13] T. M. Fortier, M. S. Kirchner, F. Quinlan, J. Taylor, J. C. Bergquist, T. Rosenband, N. Lemke, A. Ludlow, Y. Jiang, C. W. Oates, and S. A. Diddams, Nat. Photon. **5**, 425 (2011).

[14] A. Foltynowicz, P. Masłowski, T. Ban, F. Adler, K. C. Cossel, T. C. Briles, and J. Ye, Faraday Discuss. **150**, 23 (2011).

[15] K. Saha, Y. Okawachi, B. Shim, J. S. Levy, R. Salem, A. R. Johnson, M. A. Foster, M. R. Lamont, M. Lipson, and A. L. Gaeta, Opt. Express **21**, 1335 (2013).
[16] C. Godey, I. V. Balakireva, A. Coillet, and Y. K. Chembo, Phys. Rev. A **89**, 063814 (2014).
[17] T. Carmon, L. Yang, and K. J. Vahala, Opt. Express **12**, 4742 (2004).
[18] Y. Deng, F. Liu, Z. C. Leseman, and M. Hossein-Zadeh, Opt. Express **21**, 4653 (2013).
[19] X. Yi, Q.-F. Yang, K. Y. Yang, M.-G. Suh, and K. Vahala, Optica **2**, 1078 (2015).
[20] H. Tapalian, J.-P. Laine, and P. Lane, IEEE Photonics Technol. Lett. **14**, 1118 (2002).
[21] P. Del'Haye, O. Arcizet, A. Schliesser, R. Holzwarth, and T. J. Kippenberg, Phys. Rev. Lett. **101**, 053903 (2008).
[22] A. A. Savchenkov, A. B. Matsko, D. Strekalov, M. Mohageg, V. S. Ilchenko, and L. Maleki, Phys. Rev. Lett. **93**, 243905 (2004).
[23] W. Liang, V. Ilchenko, A. Savchenkov, A. Matsko, D. Seidel, and L. Maleki, Opt. Lett. **35**, 2822 (2010).
[24] F. Dehghani, S. Mohammadi, B. Barekatain, and M. Abdollahi, Nano Commun. Net. **26**, 100323 (2020).
[25] A. Pasquazi, M. Peccianti, L. Razzari, D. J. Moss, S. Coen, M. Erkintalo, Y. K. Chembo, T. Hansson, S. Wabnitz, P. Del'Haye *et al.*, Phys. Rep. **729**, 1 (2018).
[26] X. Xue, Y. Xuan, Y. Liu, P.-H. Wang, S. Chen, J. Wang, D. E. Leaird, M. Qi, and A. M. Weiner, Nat. Photon. **9**, 594 (2015).
[27] C. Joshi, J. K. Jang, K. Luke, X. Ji, S. A. Miller, A. Klenner, Y. Okawachi, M. Lipson, and A. L. Gaeta, Opt. Lett. **41**, 2565 (2016).
[28] A. Pasquazi, L. Caspani, M. Peccianti, M. Clerici, M. Ferrera, L. Razzari, D. Duchesne, B. E. Little, S. T. Chu, D. J. Moss *et al.*, Opt. Express **21**, 13333 (2013).
[29] X. Yi, Q.-F. Yang, K. Y. Yang, and K. Vahala, Opt. Lett. **41**, 2037 (2016).
[30] T. C. Briles, J. R. Stone, T. E. Drake, D. T. Spencer, C. Fredrick, Q. Li, D. Westly, B. Ilic, K. Srinivasan, S. A. Diddams *et al.*, Opt. Lett. **43**, 2933 (2018).
[31] D. C. Cole, J. R. Stone, M. Erkintalo, K. Y. Yang, X. Yi, K. J. Vahala, and S. B. Papp, Optica **5**, 1304 (2018).
[32] S. Zhang, J. M. Silver, L. Del Bino, F. Copie, M. T. Woodley, G. N. Ghalanos, A. Ø. Svela, N. Moroney, and P. Del'Haye, Optica **6**, 206 (2019).
[33] J. Liu, E. Lucas, A. S. Raja, J. He, J. Riemensberger, R. N. Wang, M. Karpov, H. Guo, R. Bouchand, and T. J. Kippenberg, Nat. Photon. **14**, 486 (2020).
[34] G. Moille, X. Lu, A. Rao, Q. Li, D. A. Westly, L. Ranzani, S. B. Papp, M. Soltani, and K. Srinivasan, Phys. Rev. Applied **12**, 034057 (2019).
[35] T. Kobatake, T. Kato, H. Itobe, Y. Nakagawa, and T. Tanabe, IEEE Photonics J. **8**, 1 (2016).
[36] J. K. Jang, A. Klenner, X. Ji, Y. Okawachi, M. Lipson, and A. L. Gaeta, Nat. Photon. **12**, 688 (2018).
[37] G. P. Agrawal, *Nonlinear Science at the Dawn of the 21st Century* (Springer, New York, 2000), pp. 195–211.
[38] K. Okamoto, *Fundamentals of Optical Waveguides* (Academic, New York, 2006).
[39] L. A. Lugiato and R. Lefever, Phys. Rev. Lett. **58**, 2209 (1987).
[40] P. Grelu, *Nonlinear Optical Cavity Dynamics: From Microresonators to Fiber Lasers* (Wiley, New York, 2015).
[41] S. Coen, H. G. Randle, T. Sylvestre, and M. Erkintalo, Opt. Lett. **38**, 37 (2013).
[42] J. Kischkat, S. Peters, B. Gruska, M. Semtsiv, M. Chashnikova, M. Klinkmüller, O. Fedosenko, S. Machulik, A. Aleksandrova, G. Monastyrskyi *et al.*, Appl. Opt. **51**, 6789 (2012).
[43] A. Kovach, D. Chen, J. He, H. Choi, A. H. Dogan, M. Ghasemkhani, H. Taheri, and A. M. Armani, Adv. Opt. Photon. **12**, 135 (2020).
[44] Y. Deng, R. Flores-Flores, R. K. Jain, and M. Hossein-Zadeh, Opt. Lett. **38**, 4413 (2013).
[45] L. He, Y.-F. Xiao, J. Zhu, S. K. Ozdemir, and L. Yang, Opt. Express **17**, 9571 (2009).
[46] A. W. Elshaari, I. E. Zadeh, K. D. Jöns, and V. Zwiller, IEEE Photonics J. **8**, 1 (2016).
[47] C. Bao, L. Zhang, A. Matsko, Y. Yan, Z. Zhao, G. Xie, A. M. Agarwal, L. C. Kimerling, J. Michel, L. Maleki *et al.*, Opt. Lett. **39**, 6126 (2014).
[48] J. K. Jang, Y. Okawachi, Y. Zhao, X. Ji, C. Joshi, M. Lipson, and A. L. Gaeta, Opt. Lett. **46**, 3657 (2021).
[49] A. B. Matsko, A. A. Savchenkov, N. Yu, and L. Maleki, J. Opt. Soc. Am. B **24**, 1324 (2007).
[50] S. Coen and M. Erkintalo, Opt. Lett. **38**, 1790 (2013).